Construction of Poincaré return maps for Rössler flow

Arindam Basu[*]
School of Electrical and Computer Engineering
Georgia Institute of Technology, Atlanta, GA 30332-250
(Dated: August 26, 2007)

A method for constructing Poincaré return maps for strongly contracting flows by coding the arc-length along the unstable manifold in a Poincaré section is proposed. This method is used to find return maps for the Rössler flow. The return map is used to partition the phase space using the itinerary of the critical point. Inadmissible itineraries are pruned using kneading theory, and admissible prime cycles up to length 9 are tabulated. The effects of finite computational accuracy and errors in curve-fitting are treated as white noise to compute the limit of phase space partitioning. A Markov diagram is constructed for generating the admissible itineraries till this limit. The cycles of the Rössler flow are found using inverse iteration methods and corresponding cycle-stability values are tabulated. Finally the Lyapunov exponent is computed using periodic orbit theory and verified by numerical integration of the flow.

I. INTRODUCTION

Analyzing the dynamics of a high dimensional flow in the corresponding phase space is a non-trivial task. Conventionally, instead of analyzing the continuous flow, we observe the dynamics induced by the flow on a particular section of the phase space. The chosen section is the called the Poincaré section and helps in visualizing the problem. Typically a discrete mapping is derived from the successive intersections of the flow with the section to produce the return map.

This project investigates how to construct a good Poincaré return map for a 3-dimensional Rössler flow, with an eye on how the problem is solved for higher-dimensional systems.

The concept of a Poincaré section is introduced in sect. II. The Rössler flow and typical Poincaré sections are described in sect. III. In sect. IV we show that for the Rössler flow the Poincaré return maps are well approximated by 1-d mappings. Our method for computing return maps based on unstable manifold is explained, together with details of numerical implementation. Details of computation of admissible itineraries using symbolic dynamics and kneading theory is presented in sect. V. The Markov diagram and the transition matrix for the map is derived. In sect. VII we search for the solutions (x, T), $x \in \mathbb{R}^d$, $T \in \mathbb{R}$ of the *periodic orbit condition*

$$f^{t+T}(x) = f^t(x), \qquad T > 0 \qquad (1)$$

for the Rössler flow using the information from the symbolic dynamics machinery developed earlier. Periodic orbits are listed with their stabilities and return times.

Finally these orbits are used to compute the Lyapunov exponent using Periodic Orbit Theory.

Some of the background text is taken verbatim from ref. [1]. This report and the programs used in its preparation are available on `ChaosBook.org` [2].

II. POINCARÉ SECTIONS

Successive trajectory intersections with a *Poincaré section*, a $(d-1)$-dimensional hypersurface or a set of hypersurfaces $\mathcal{P}$ embedded in the d-dimensional phase space $\mathcal{M}$, define the *Poincaré return map* $P(x)$, a d-dimensional map of form

$$x' = P(x) = f^{\tau(x)}(x), \qquad x', x \in \mathcal{P}. \qquad (2)$$

Here the *first return function* $\tau(x)$ is the time of flight to the next section for a trajectory starting at x. The choice of the section hypersurface $\mathcal{P}$ is altogether arbitrary. The hypersurface can be specified implicitly through a function $U(x)$ that is zero whenever a point x is on the Poincaré section,

$$x \in \mathcal{P} \quad \text{iff} \quad U(x). \qquad (3)$$

The gradient of $U(x)$ evaluated at $x \in \mathcal{P}$ serves a twofold function. First, the flow should pierce the hypersurface $\mathcal{P}$, rather than being tangent to it. A nearby point $x + \delta x$ is in the hypersurface $\mathcal{P}$ if $U(x + \delta x) = 0$. A nearby point on the trajectory is given by $\delta x = v \delta t$, so a traversal is ensured by the *transversality condition*

$$(v \cdot \partial U) = \sum_{j=1}^{d} v_j(x) \partial_j U(x) \neq 0, \quad x \in \mathcal{P}. \qquad (4)$$

Second, the gradient $\partial_j U$ defines the orientation of the hypersurface $\mathcal{P}$. The flow is oriented as well, and a periodic orbit can pierce $\mathcal{P}$ twice, traversing it in either

[*]Electronic address: abasu3 [snail] mail.gatech.edu
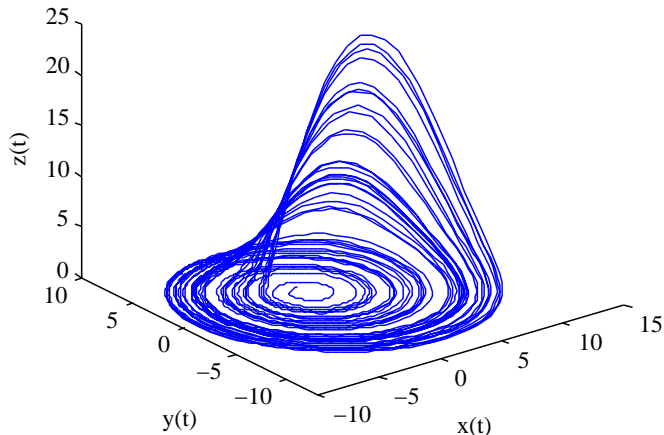- available on `ChaosBook.org/projects`

FIG. 1: The strange attractor for the Rössler flow (6).

direction. Hence the definition of Poincaré return map $P(x)$ needs to be supplemented with the orientation condition

$$\sum_{j=1}^{d} v_j(x_n)\partial_j U(x_n) > 0 \,. \tag{5}$$

In this way the continuous time t flow $f^t(x)$ is reduced to a discrete time n sequence x_n of successive oriented trajectory traversals of $\mathcal{P}$. However, visualization of high dimensional maps can a challenge. The problem can be simplified to a lower dimensional map if the system is dissipative and the flow strongly contracting.

III.   RÖSSLER FLOW

The Rössler flow(6) is given by the following set of differential equations:

$$\begin{aligned}
\dot{x} &= -y - z \\
\dot{y} &= x + ay \\
\dot{z} &= b + z(x - c) \,.
\end{aligned} \tag{6}$$

In all calculations that follow we shall use Rössler's parameter values $a = b = 0.2$, $c = 5.7$. Consider Fig. 1, a typical trajectory of the 3-dimensional Rössler flow (6).

It wraps around the z axis, so a good choice for a Poincaré section is a plane passing through the z axis.

A sequence of such Poincaré sections placed radially at increasing angles with respect to the x axis, Fig. 2, illustrates the stretch and fold action of the Rössler flow. To orient yourself, compare this with Fig. 1, and note the different z-axis scales. Figure 2 assembles these sections into a series of snapshots of the flow.

Once a particular Poincaré section is picked, we can also exhibit the return map (2), as in Fig. 2. Cases (g)
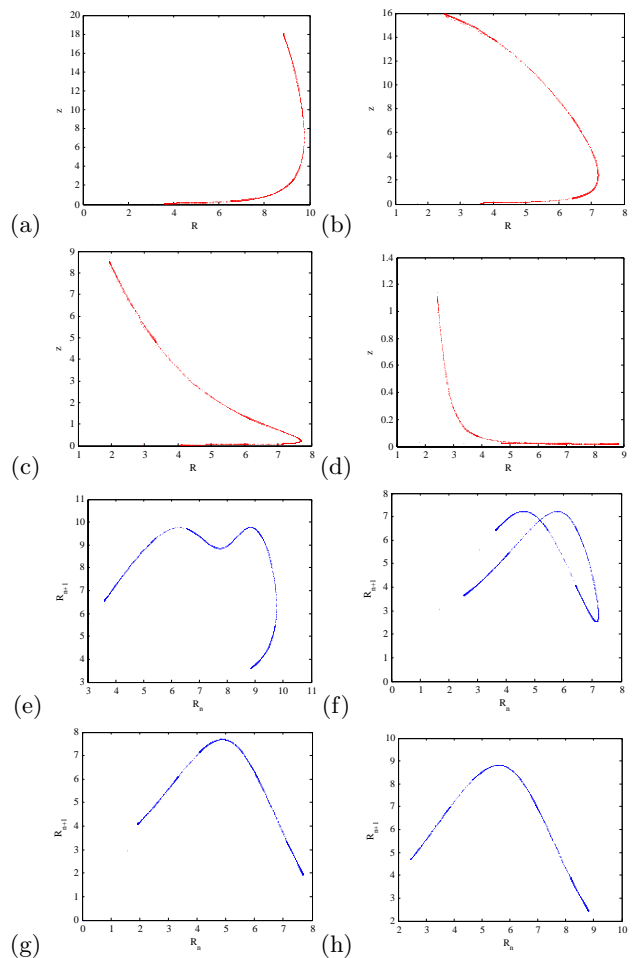

FIG. 2:   (a)-(d) Poincaré sections of the Rössler flow at $0°, 45°, 90°$ and $135°$ with respect to the x-axis. (e)-(h) Return maps for the $R_n \to R_{n+1}$ radial distance for the Poincaré sections of (a)-(d).

and (h) are examples of nice 1-to-1 return maps. However, (e) and (f) appear multimodal and non-invertible, artifacts of projection of the 2-d return map $(R_n, z_n) \to (R_{n+1}, z_{n+1})$ onto a 1-d subspace $R_n \to R_{n+1}$.

The above examples illustrate why a Poincaré section gives a more informative snapshot of the flow than the full flow portrait. For example, while the full flow portrait of the Rössler flow Fig. 1 gives us no sense of the thickness of the attractor, we see clearly in the Fig. 2 Poincaré sections that even though the return map is 2-$d \to$ 2-d, the flow contraction is so strong that for all practical purposes it renders the return map 1-dimensional.

IV.   RETURN MAP

For strongly contracting flows like Rössler, an geometrically intrinsic way to get a 1-dimensional map which encodes the dynamics of the system is to follow the unstable manifold. The unstable manifold is an invariant

FIG. 3: The two possible ways in which wrong radius of curvature might be computed.
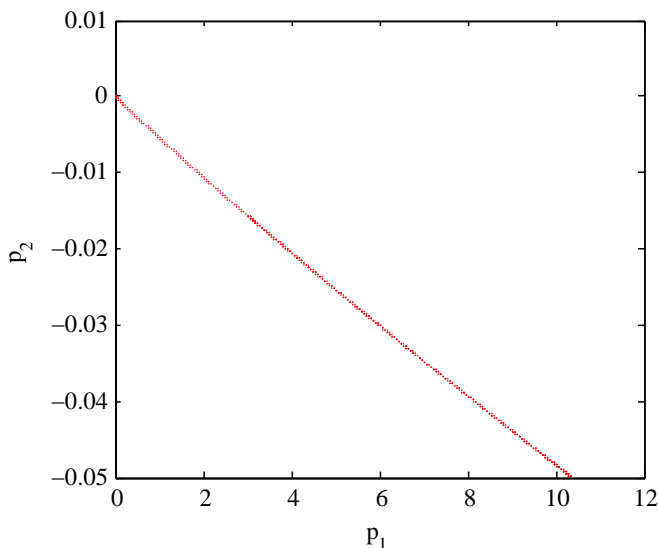
FIG. 4: The Poincaré section for the Rössler flow (6), obtained by taking as the section the plane through the inner equilibrium (x^-, y^-, z^-) in (10), with normal vector V_2 given in (12). The figure axes are projections on the orthonormal vectors P_1 and P_2 in the plane.

The method described above is used to find the Póincare section and return map for the Rössler flow (6). The flow has 2 equilibrium points given by

$$(x^-, y^-, z^-) = (0.0070, -0.0351, 0.0351)$$
$$(x^+, y^+, z^+) = (5.6929, -28.464, 28.464). \tag{10}$$

Trajectories that start out on the far side of the stable manifold of the outer equilibrium, (x^+, y^+, z^+) escape, while those that start on the inner side spiral towards the
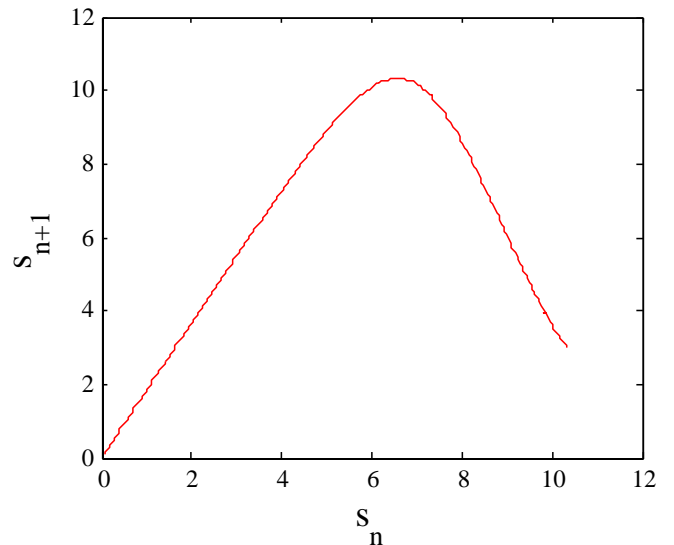
FIG. 5: The Poincaré return map for the Rössler flow (6), obtained by fixing the Poincaré section to be the plane through the inner equilibrium point, with normal vector V_2.

inner equilibrium point. Thus the stable manifold of the outer equilibrium serves as the basin boundary. Consider now the eigenvalues of the inner equilibrium point, "-"

$$(\mu_1^-, \mu_2^- \pm i\nu_2^-) = (-5.7, 0.097 \pm 0.99) \tag{11}$$

One of the eigenvectors corresponding to the complex eigenvalues is

$$V_2 = (0.70728, -0.072725, 0.0041683). \tag{12}$$

We define a Poincaré section by the plane passing through (x^-, y^-, z^-) and normal to V_2. Figure 4 shows the section of the flow with the axes being two orthonormal vectors in the plane given by

$$\begin{aligned} P_1 &= (-0.1023757, -0.994738, 0.0038795) \\ P_2 &= (-0.005434, 0.0044592, 0.9999752). \end{aligned} \tag{13}$$

The plot exhibits the strong contraction along the z direction, and surprisingly little nonlinearity between the equilibrium point at $p_1 = 0$, where linear approximation is valid, and the slope is given exactly by .... , and $p_1 = 10$, where the unstable manifold is far in the nonlinear part of the dynamics as it can possibly be. The corresponding Poincaré return map is plotted in Fig. 5.

V.   KNEADING SEQUENCE

The unimodal return map allows us to use symbolic dynamics to partition the phase space by assigning labels to neighborhoods of cycle points [1]. Finite Markov graphs or finite automata for unimodal maps are discussed in ref. [3]. They belong to the category of regular

languages. A good hands-on introduction to symbolic dynamics is given in ref. [4].

The phase space is initially partitioned in two sections by points to the right of the critical point (label "1") and points on the left (label "0"). In the second iteration, each of these partitions are refined to get four partitions, "00","01","11" and "10", based on two step itineraries of points and so on. These time-based itineraries, s_n, can be converted to their corresponding spatial ordering, γ using the kneading rule, K, given by

$$
\begin{aligned}
w_{n+1} &= w_n, & s_{n+1} = 0 \\
&= 1 - w_n, & s_{n+1} = 1.
\end{aligned}
$$

The cause of this reversal is the folding nature of the map to the right of the critical point. Thus given any itinerary of binary values, S, we can specify the topological coordinate by evaluating $\gamma = K(S)$.

A. Admissible itineraries

At the nth level, we can have a maximum of 2^n partitions, but not all of them will be allowed by the dynamics. Kneading theory for unimodal maps enables us to determine the admissible itineraries by from the itinerary S_c of the critical point. The critical $f(x_c)$ is the rightmost point visited by the dynamics, with the corresponding kneading value $\kappa = K(S_c)$. As we are interested in the non-wandering set of points, cycles which visit a topological coordinate larger than κ cannot belong to the non-wandering set for that map and are pruned. In the Rössler example investigated here, the itinerary of the critical point and its kneading value are:

$$
\begin{aligned}
S_c &= 0.100101111\cdots, \\
\kappa &= 0.111001010\cdots. \quad (14)
\end{aligned}
$$

Note that due to finite precision in computation the itinerary of the critical point is always going to be a cycle. In this case, we found it to be a 13-cycle. To find the topological coordinate of a p-cycle, we need to account for the fact that it is an infinite string. Thus if the p cycle itinerary repeating block has value D_p, its coordinate is given by:

$$
\gamma_p = \frac{D_p}{1 - 2^{-p}}
$$

Table I lists all admissible prime cycles of topological length $n \leq 9$ allowed by the kneading sequence (14). In contrast to the tent map, the dike map can have stable cycles, and its dynamics is closer to smooth unimodal maps for whom chaotic parameter regions are densely interspersed with stability windows. The itinerary of the critical point is preperiodic to a stable cycle if it falls into the flat-top region of the dike map.
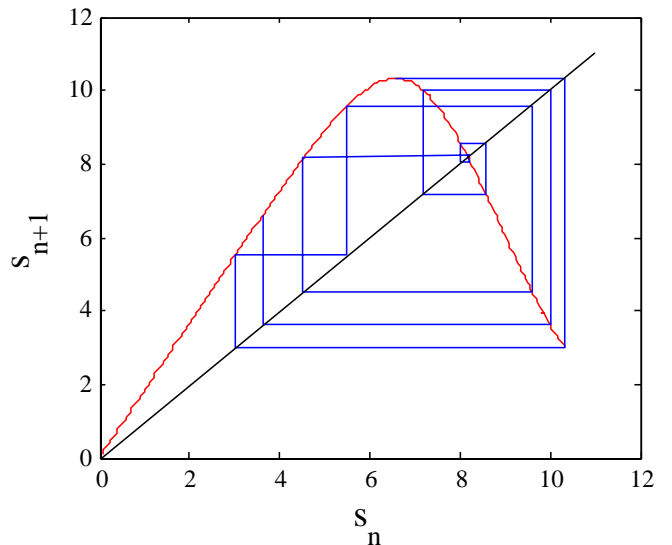
FIG. 6: The itinerary of the critical point, Rössler return map Fig. 5.
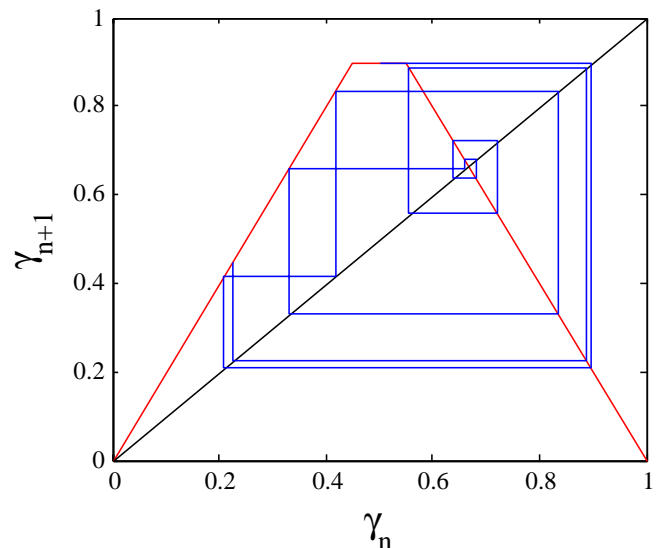
FIG. 7: The dike map of height κ computed in (14), with the same critical point itinerary as the Rössler return map Fig. 5.

B. Markov diagrams

The Markov diagram representation of a topological dynamics allows one to compactly generate all admissible itineraries. The compactness of the representation arises from the fact that it encodes the finite memory self-similarities in the admissible symbol-sequences trees for the given dynamical system. To construct a Markov diagram, we need to specify a grammar for the symbolic representation of dynamics. Here we construct the grammar from the unimodal maps pruning rule: no infinite symbolic itinerary may have a sub-block whose spatial

TABLE I: Admissible cycles for the Rössler flow of length $n \leq 9$.

Length	Cycle	Length	Cycle	Length	Cycle
1	0	2	01	3	001
	1				011
4	0111	5	01011	6	001011
			01111		010111
					011111
7	0101011	8	00100101	9	001001011
	0101111		00100111		001001101
	0110111		00101101		001001111
	0111111		00101111		001011011
			01010111		010110111
			01011011		011011111
			01011111		011101111
			01101111		011111111
			01111111		

(a)

(b)

(c)

(d)

FIG. 8: A Markov diagram for the Rössler flow with the kneading value truncated to 6 digits. The pruning blocks in this case are ␣1000␣ and ␣10011␣. (a) Starting with the start node "." delineate all pruning blocks on the binary tree. A solid line stands for "1" and a dashed line stands for "0". Ends of inadmissible strings are marked with ×. Label all internal nodes by reading the symbols connecting "." and the node. (b) Indicate all admissible starting blocks by arrows. (c) Drop recursively the leading symbols in the admissible blocks; if the truncated string corresponds to an internal node in (a), connect them. (d) Delete the transient nodes.

topological coordinate is greater than κ_c. For practical implementation however, we truncate κ_c to a finite number of digits (corresponding to finite memory) to generate a graph with finite number of nodes. An inadmissible symbol sequence of n symbols corresponds to the starting point of a partition at the nth level that is to the right of κ. Not all points in the previous interval are admissible, but the finite calculation precision limits evaluation of further pruning rules.

At 6th step, the kneading sequence blocks prunes blocks ␣100111␣, ␣100110␣, ␣100010␣, ␣100011␣, ␣100001␣ and ␣100000␣. These can be grouped under two pruning rules as the first two inadmissible blocks have same digits in first five places and the next four inadmissible blocks have same digits in first four places. All of the above result in two inadmissible blocks: ␣1000␣ and ␣10011␣. Construction of the Markov diagram is shown in Fig. 8. Draw the pruning tree as a section of a binary tree with 0 and 1 branches and label each internal node by the sequence of 0's and 1's connecting it to the root of the tree. These are the potentially dangerous nodes - beginning of blocks that might end up pruned. Add the side branches to those nodes. As we continue down such branches we have to check whether the pruning imposes constraints on the sequences so generated. We do this by knocking off the leading symbols and checking whether the shortened strings coincide with any of the internal pruning tree nodes: 11→1; 101→01→1; 10010→0010→010→10. The trees originating in identified nodes are self-similar. Now connect the side branches to the corresponding nodes. Nodes "." and "0" are transient nodes where the dynamics does not return. Hence they are removed to get the final Markov graph.

C. Topological entropy

From the Markov diagram, one can easily get the corresponding transition matrix. Since there are four distinct nodes in the Markov graph, the transition matrix is a 4×4 matrix given by:

$$\begin{pmatrix} 1 & 1 & 0 & 0 \\ 0 & 0 & 0 & 1 \\ 0 & 1 & 0 & 0 \\ 0 & 0 & 1 & 0 \end{pmatrix} \tag{15}$$

The matrix is a Perron matrix as it should be because the Markov graph is fully connected. The trace of the transition matrix multiplied "n" times, A^n, gives the number of possible n-cycle points, N_n. The relation between N_n

and the topological entropy, h_top is given by:

$$N_n = e^{h \cdot n} \tag{16}$$

As the transition matrix is a Perron matrix, we know it has a positive eigenvalue which is strictly larger than the other eigenvalues. This property allows us to compute the topological entropy as:

$$h_{top} = ln(\lambda_{max}) = ln(1.7221) = 0.5435 \tag{17}$$

From the Markov graph, we can also create the corresponding topological zeta function by considering products of non self-intersecting loops as described in ref. [1] to get:

$$\frac{1}{\zeta_{top}} = 1 - t_1 - t_{01} - t_{001} + t_1 t_{001} = 1 - z - z^2 - z^3 + z^4 \tag{18}$$

The topological entropy obtained from the leading zero of this polynomial also matches with the previously computed value.

VI.   THE BEST POSSIBLE PARTITION

In all discussions of symbolic dynamics till now, we have considered infinite precision in computing pre-images which is definitely not the case in real implementations. The kneading value for the critical point depends on the accuracy of the Poincaré return map, inaccuracies arising due to interpolation errors between the finite number of data points considered and round-off errors. Resolution in computing the kneading value is limited to the step, n_{knead} in which the inaccuracy in obtaining the next symbol in the kneading trajectory is higher than a certain threshold. We can then compute admissible cycles only till this accuracy.

To find the admissible partitions, we need to find the pre-images of the critical point, x_c. For unimodal maps like this, the interesting region is bounded by $f(x_c)$ and $f(f(x_c))$. One stops partitioning at the step n_{part} when two intervals overlap more than a certain threshold. It is not necessary that all intervals overlap at this point. So intervals which do not overlap may be further refined.

Then one determines all prime cycles for that partition, nothing beyond. They correspond to all non-self intersecting loops on the corresponding Markov diagram.

To find the accuracy limits, we first consider a gaussian probability distribution centered around the critical point, x_c given by:

$$\rho_0(x) = C_0 e^{-(\beta_0(x - x_c))^2}, \tag{19}$$

where β_0 models models the inaccuracy in knowing the critical point. So instead of iterating a point, we now iterate a density of points. The effect of the noisy mapping is included by using the Fokker-Planck evolution operator, L_D, instead of the Perron-Frobenius operator :

$$L_D \rho(x) = \frac{1}{4\pi D} \int dy e^{\frac{-(x - f(y))^2}{4D}} \rho(y) \tag{20}$$
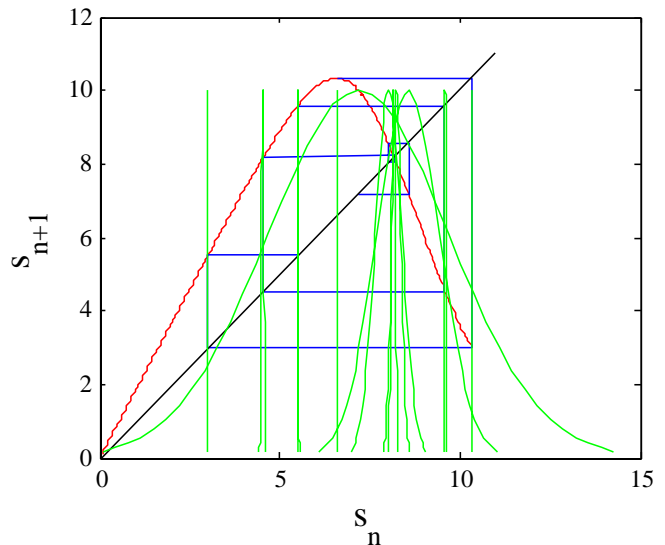
FIG. 9: Forward evolution of a gaussian centered around the critical point with $\beta = 10^3$. The number of digits in the kneading trajectory is 10.

where D is the variance of the noise. The noisy evolution is represented by replacing the delta function in the kernel of the Perron-Frobenius operator with a gaussian. Similarly, one can get the operator for backward evolution by considering the adjoint of the Fokker-Planck evolution operator, $L_D^\dagger$ given by:

$$L_D^\dagger \rho(x) = \int_{-\infty}^{\infty} dy e^{\frac{-(f(x) - y)^2}{4D}} \rho(y) \tag{21}$$

Thus we now get a convolution of a gaussian with a gaussian. Since we know that the result of this convolution is another gaussian, we can find a recursion relation between the widths of the densities iterated forward and backward in time. For the forward iteration, we get:

$$\beta_{n+1}^2 = \frac{\beta_n^2}{4D\beta_n^2 + f'^2(x_n)} \tag{22}$$

and for the backward iteration we get:

$$\beta_{-(n+1)} = \frac{f'^2(f^{-1}(x_{-n}))\beta_{-n}}{1 + 4D\beta_{-n}} \tag{23}$$

The stopping condition was taken as the distance between centres of two gaussians being lesser than the sum of their respective half-widths.

Figure 9 shows the evolution of a gaussian forward in time till it significantly overlaps across the critical point into both regions. The number of digits in this case with $\beta = 10^3$ is 10. The number of digits for a case with $\beta = 10^8$ is 13. The number of digits does not improve beyond this as the critical point is part of a 13-cycle and so after 13 iterations the gaussian spills into both regions. Figure 10 shows the partitioning of the phase
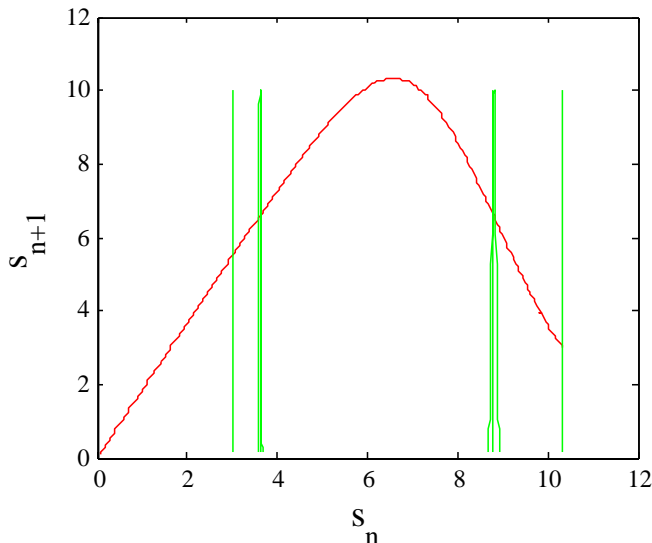
FIG. 10: Backward evolution of a gaussian centered around the critical point with $\beta = 10^3$. The number of partitions before two Gaussians overlap is 5.

space before overlap between any two regions occur. The two Gaussians at the two borders are centered around the two future iterates of the critical point while the others are backward iterates of the critical point. The number of non-overlapping partitions obtained with $\beta = 10^3$ is 5.

VII. WHERE ARE THE CYCLES?

In this section, we search for the solutions (x, T), $x \in \mathbb{R}^d$, $T \in \mathbb{R}$ of the *periodic orbit condition*

$$f^{t+T}(x) = f^t(x), \qquad T > 0 \qquad (24)$$

for a given flow or mapping.

A *prime* cycle p of period T_p is a single traversal of the periodic orbit, so our task will be to find a cycle point $x \in p$ and the shortest time T_p for which (24) has a solution. A cycle point of a flow f^t which crosses a Poincaré section n_p times is a fixed point of the P_p^n iterate of the Poincaré section return map P, hence we shall refer to all cycles as "fixed points". By cyclic invariance, stability eigenvalues and the period of the cycle are independent of the choice of the initial point, so it will suffice to solve (24) at a single cycle point.

If the cycle is an attracting limit cycle with a sizable basin of attraction, it can be found by integrating the flow for sufficiently long time. If the cycle is unstable, simple integration forward in time will not reveal it. Due to the exponential divergence of nearby trajectories in chaotic dynamical systems, fixed point searches based on direct solution of the fixed-point condition (24) as an initial value problem can be numerically very unstable.

Methods that start with initial guesses for a number of points along the cycle, such as the multipoint shooting

method and the variational methods, are considerably more robust and safer.

A prerequisite for any exhaustive cycle search is a good understanding of the topology of the flow: a preliminary step to any serious periodic orbit calculation is preparation of a list of all distinct admissible prime periodic symbol sequences, such as the list given in Table I. The relations between the temporal symbol sequences and the spatial layout of the topologically distinct regions of the state space enable us to guess location of a series of periodic points along a cycle. As the return maps found earlier were very nicely approximated by 1 dimensional mappings, we next outline a few methods to get cycle points from such maps.

A. Newton's method

Newton's method for determining a zero x^* of a function $F(x)$ of one variable is based on a linearization around a starting guess x_0:

$$F(x) \approx F(x_0) + F'(x_0)(x - x_0). \qquad (25)$$

An approximate solution x_1 of $F(x) = 0$ is

$$x_1 = x_0 - F(x_0)/F'(x_0). \qquad (26)$$

The approximate solution can then be used as a new starting guess in an iterative process. A fixed point of a map f is a solution to $F(x) = x - f(x) = 0$. We determine x by iterating

$$
\begin{aligned}
x_m &= g(x_{m-1}) = x_{m-1} - F(x_{m-1})/F'(x_{m-1}) \\
&= x_{m-1} - \frac{1}{1 - f'(x_{m-1})}(x_{m-1} - f(x_{m-1})) .(27)
\end{aligned}
$$

B. Inverse iteration

We find the unstable cycles of Rössler return map Fig. 5 by the very simple inverse map method: unstable cycles of 1-d maps are attracting cycles of the inverse map. The inverse map is not single valued, so at each backward iteration we have a choice of branch to make. By choosing branch according to the symbolic dynamics of the cycle we are trying to find, we converge to the desired cycle. The rate of convergence is given by the stability of the cycle, that is, the convergence is exponentially fast. Figure 11 shows such paths to the $\overline{01011}$ and $\overline{01111}$-cycles.

The values obtained in this manner correspond to arc-length along the manifold. From this information, we can get back the point in the Poincaré section that corresponds to the cycle. As an example, consider the fixed point with symbolic dynamics label $\overline{1}$. From the map, we find its corresponding arc-length is $s_1 = 8.181006$ to get the Poincaré section point $(0, y_1, z_1)$. The period T_1,
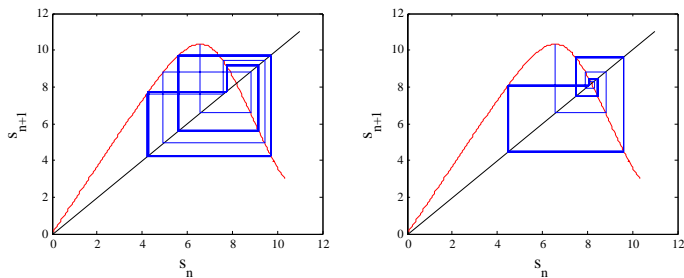
FIG. 11: The inverse iteration method converges to the two admissible 5-cycles $\overline{01011}$ and $\overline{01111}$. The symbol sequence can be read off from the figures directly by noting that the critical point demarcates the border between intervals "0" and "1".

TABLE II: The short Rössler cycles, together with a Poincarè section cycle point, cycle expanding eigenvalue cycle period and error.

n_p	p	x_p	y_p	z_p	Λ_p	T_p	D_p
1	1	-.8302	-8.172	.02675	-2.42729	5.881170	2.05e-6
2	01	-.5331	-5.285	.02898	-3.522737	11.75676	8.74e-6
3	001	-.9951	-9.775	.02571	-2.347972	17.50960	1.46e-7
	011	-.5331	-5.285	.02898	5.225288	17.59147	9.55e-6
4	0111	-.4741	-4.711	.02948	-16.74413	23.51310	2.43e-5
5	01011	-.4300	-4.283	.02989	-23.66509	29.35742	4.12e-6
	01111	-.4507	-4.484	.02970	35.89404	29.39955	2.86e-5

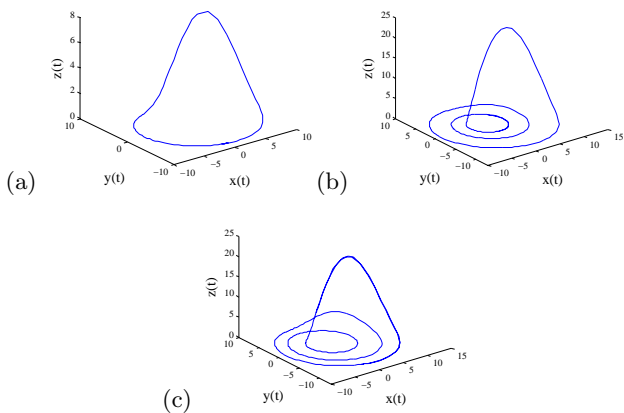FIG. 12: Rössler 3-d cycles found by inverse iteration of Fig. 5, with trajectory integrated from each cycle point to the first Poincaré section return: (a) $\overline{1}$-cycle (b) $\overline{001}$-cycle (c) $\overline{011}$-cycle.

TABLE III: The Rössler system: the itinerary p, a periodic point $x_p = (0, y_p, z_p)$ and the expanding eigenvalue Λ_p for all cycles up to the topological length 5. (Joachim Mathiesen)

n_p	p	y_p	z_p	Λ_e
1	1	6.091768319	1.29973193	-2.4039535318268
2	01	3.91580404	3.69283338	-3.5120069815161
3	001	2.27828103	7.4164809	-2.3419235232340
	011	2.93287755	5.67080594	5.3449081538885
4	0111	3.46675871	4.50621753	-16.6967406980700
5	01011	4.16279878	3.30390333	-23.1995830097831
	01111	3.27891435	4.89045292	36.8863297988981

For comparison with Table II Joachim Mathiesen's Table III from `ChaosBook.org` tabulates all admissible prime cycles to $n = 5$, determined by Newton method.

C. Linear stability

An estimate of the stability of a Rössler cycle is obtained multiplying the slopes of the 1-d return map Fig. 5 at the cycle points:

$$\Lambda(s_0, n) = \frac{d}{ds} S^n(s_0) = \prod_{m=0}^{n-1} S'(s_m), \quad s_m = S^m(s_0). \tag{29}$$

The stabilities of the cycles so derived are tabulated in Table II and match closely with the ones computed by Joachim Mathiesen tabulated in Table III.

As an application, of periodic orbit theory, we calculate the Lyapunov exponent using numerical techniques and compare it with the value obtained from the periodic orbits. Figure 13 shows the logarithm of the increasing separation of the distance between two points plotted against time. When the separation reaches a threshold, it is reset to δr_0 again to prevent its saturation. Let δr_i be the separation before reset and t_i be the time for which the integration was done between two resets. Then we compute the Lyapunov exponent λ, a measure of local

expanding stability eigenvalues $\Lambda_{p,e}$ and Lyapunov exponent $\lambda_{p,e}$:

$$\overline{1}\text{-cycle: } (x,y,z) = (-.8302326, -8.172687, .02675678)$$
$$T_1 = 5.88117$$
$$\Lambda_{1,e} = -2.42729$$
$$\lambda_{1,e} = 0.15076. \tag{28}$$

Figure 12 (a) shows the computed $\overline{1}$-cycle. Figure 12 (b)-(c) shows two examples of computation of longer cycles. Table II tabulates all admissible prime cycles till a topological length of 5, one of their points on the Poincarè section, their expanding eigenvalue, period of the cycle and the numerical error in the computation quoted as an effective diffusion constant.

The numerical round-off errors along a trajectory are uncorrelated, acting as noise, so the error sum $E_p = \sum_{k=1}^{n_p}(x_{k+1} - f(x_k))^2$ is expected to grow as the sum of squares of uncorrelated steps, linearly with time. Hence the numerical noise is characterized by an effective "diffusion constant" $D_p = E_p/2dn_p$. Cycle-by-cycle D_p evaluated in Table II show a surprising spread.
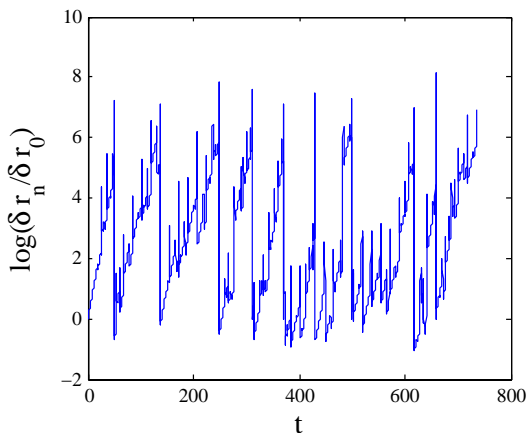
FIG. 13: The logarithm of the ratio of separation between two points initially separated by δr_0 is plotted against time. When the separation reaches a threshold, it is reset to δr_0 again to prevent its saturation. The Lyapunov exponent computed from this is $\lambda = 0.10036\pm?$.

TABLE IV: The cycle expansion terms for Rössler till order 5.

n_p	Cycle Expansion
1	$-t_1$
2	$-t_{01}$
3	$-(t_{011} - t_{01}t_1) - t_{001}$
4	$-(t_{0111} - t_{011}t_1) + t_{001}t_1$
5	$-(t_{01011} - t_{011}t_{01}) - (t_{01111} - t_{0111}t_1) + t_{001}t_{01}$

instability, as:

$$\lambda = \frac{\sum_i log(\delta r_i/\delta r_0)}{\sum_i t_i} \quad (30)$$

The above calculation gives the Lyapunov exponent to be $\lambda = 0.10036\pm?$.

The cycle expansion for this system is expanded in increasing order in Table IV. As can be seen, higher order terms are shadowed by some lower order ones and so the first few cycles give the major contribution to all computations while higher ones allow for curvature corrections. Now, we calculate the Lyapunov exponent as an average from the cycle averaging formula from [1] given by:

$$\lambda = \frac{1}{<n>_\zeta} \sum_\pi (-1)^{k+1} \frac{log|\Lambda_{p1}| + ...log|\Lambda_{p_k}|}{|\Lambda_{p1}...\Lambda_{p_k}|}, \quad (31)$$

where the cycle mean is found from

$$<n>_\zeta = \sum_\pi (-1)^{k+1} \frac{n_{p1} + ...n_{pk}}{|\Lambda_{p1}...\Lambda_{p_k}|}. \quad (32)$$

To compare with the Lyapunov exponent computed earlier, we need to estimate the average return time between consecutive intersections of the poincaré section. This can be done by plugging in the T_p values in Table II in place of n_p in the formula for $<n>_\zeta$ to get $T_p \approx 5.81$. The Lyapunov exponent computed this way is 0.081 which is close to the earlier value.

VIII. DISCUSSION

In order to reduce the dimensionality of the Poincaré return maps in strongly contracting high dimensional flows where the attractor is approximately a thin curve, we introduced a method of finding the return map based on measuring lengths along the unstable manifold. The main concept is based on finding the *"turnback"* points, that is, points where the unstable manifold changes direction due to folding. This is achieved by measuring curvature of the manifold.

This was applied to the Rössler flow to obtain a return map and guess the covering symbolic dynamics. Interestingly, this flow has a very high contraction leading to extremely large curvatures which renders the curvature computation infeasible. An alternate method has been developed for such highly contracting flows. Allowed cycles were correctly predicted by this method and the topological entropy based on the zeta function or the Markov graph could be calculated. It should be noted that the derivatives needed for all computations need to be smoothed for good computational accuracy.

[1] P. Cvitanović, R. Artuso, R. Mainieri, G. Tanner, and G. Vattay, *Chaos: Classical and Quantum* (Niels Bohr Institute, Copenhagen, 2007), `ChaosBook.org`.

[2] A. Basu (2007), term project for PHYS 6268 course "Chaos, and what to do about it", URL `ChaosBook.org/projects/#Basu`.

[3] P. Grassberger, Z. Naturforsch. A **43**, 671 (1988).

[4] D. Lind and B. Marcus, *An introduction to symbolic dynamics and coding* (Cambridge University Press, Cambridge, 1995).